electronics

MDPI

Article

Fast Hybrid Computational Technique for the Analysis of Radome Structures Using Dual Domain Decomposition

Carlos Delgado [1,*], Eliseo García [2] and Felipe Cátedra [1]

[1] Computer Science Department, Universidad de Alcalá, 28805 Alcala de Henares, Spain; felipe.catedra@uah.es
[2] Automatics Department, Universidad de Alcalá, 28805 Alcala de Henares, Spain; eliseo.garcia@uah.es
* Correspondence: carlos.delgado@uah.es

Abstract: This work details a technique tailored to the analysis of complex radome structures based on the non-overlapping separation of two different domains: antenna and radome. Both domains are analyzed isolated using the method of moments with the multilevel fast multipole algorithm (MoM-MLFMA) for the antenna domain and a modified characteristic basis function method with the multilevel fast multipole algorithm approach for the radome domain. An iterative procedure is then applied to compute the effect of each domain over the complementary domain. This approach usually converges into a few iterations, yielding very good results and significant efficiency improvements with respect to other efficient approaches such as a full-wave MoM-MLFMA analysis of the full problem. A realistic test case is included, considering a radome with an embedded frequency selective structure on one of its interfaces. The results show a very good agreement considering only three iterations between domains, requiring only one-third of the CPU-time needed by the conventional approach.

Keywords: radome; macro basis functions; method of moments; electromagnetic analysis

check for updates

Citation: Delgado, C.; García, E.; Cátedra, F. Fast Hybrid Computational Technique for the Analysis of Radome Structures Using Dual Domain Decomposition. *Electronics* **2021**, *10*, 2196. https://doi.org/10.3390/electronics10182196

Academic Editor: Andrea Randazzo

Received: 19 July 2021
Accepted: 27 August 2021
Published: 8 September 2021

1. Introduction

Radomes are weatherproof structures that protect an antenna from several external factors such as ice, rain, or debris, as well as serving in some cases as a protective barrier for personnel who work near fast-rotating elements. In some applications, the radome contributes to the aerodynamic properties of the platform (e.g., aircrafts). Radomes are used with many common industrial purposes [1–3], such as telecommunications, vehicular, maritime or automotive applications, defense systems, air traffic control, satellite communications, aircrafts, and more. It is a part of the antenna system [4–9], which can seriously affect and degrade the transmitted and received signals, and is a key element on the radar cross section (RCS) [10] of the platform on which it is mounted. Different types of radomes can be applied with either monolithic [11] or multilayered configurations [12,13] (e.g., A-, B-, or C-type sandwich radomes). More advanced designs include frequency selective surfaces (FSSs) embedded within the inner, outer, or intermediate interfaces of the radome [14–16], where the term interface refers to a surface that separates two different media. Some factors introduced by the radome can affect the behavior of the antenna, such as dissipative losses within a dielectric material, electrical phase shifts introduced by the radome, or internal reflections between the antenna and radome or even between different parts of the radome itself. Some performance parameters to be considered with the introduction of the radome structure are the insertion losses; effect on the antenna sidelobe levels; boresight error; and, for some applications, the effect on the RCS.

Complex radomes commonly have long and costly development cycles. Prototyping, testing, and production are a large percentage of this cost. Therefore, simulation can significantly reduce development time and costs, although the analysis of complex antennas with the corresponding covering radomes can pose a formidable computational challenge [17,18] owing to the electrical size of the problem as well as convergence difficulties arising from the presence of the dielectric layers [19] and, especially, from small mesh elements corresponding to the FSS embedded within one or more interfaces. It is common to find works that combine asymptotic approaches such as physical optics (PO) [20] with rigorous techniques for the analysis of this type of structure. The iterative physical optics–boundary integral–finite element method (IPO-BI-FEM) has been used to study a sandwich tangent-ogive radome [21]. The dyadic Green's function technique combined with PO is applied to obtain the radiation pattern of a hemispherical radome fed from a circular aperture in [22]. A large single-layer FSS radome is analyzed using PO in [23]. Multilayered radomes including FSS are addressed in [24] using PO in combination with a ray-tracing technique. The full-wave analysis of complex multilayered radomes with FSS seems, however, to be lacking in the literature owing to the computational challenge involved.

There are a number of efficient variations of the method of moments [25] used to reduce the computational requirements to analyze large problems. The multilevel fast multipole algorithm (MLFMA) [26] is a well-known approach that allows fast matrix-vector products in the iterative solution process, avoiding storing the far-field coupling matrix coefficients. The MLFMA is combined with the characteristic basis function method (CBFM) in [27], which reduces the number of unknowns of the problem about one order of magnitude. The definition of macro-basis functions, which, in the context of the CBFM, are called characteristic basis functions (CBFs), requires additional CPU-time, but makes the solution process faster. It is possible to apply ray-tracing-based algorithms to selectively assign more CBFs in those parts of the geometry more prone to having a stronger contribution to the final radiated field [28], or discard those parts of the geometry with negligible contributions [29]. Domain decomposition (DD) [30] approaches offer an additional strategy for the reduction of the computational burden imposed by large problems that consist of the separation of different domains and analyze each domain separately, after which it is necessary to transfer information related to the results computed in an iterative fashion.

This work describes a full-wave analysis technique focused on the analysis of complex multilayered radomes containing FSS, by means of a dual domain decomposition scheme where the antenna and radome domains are analyzed using a combination of the CBFM and the MLFMA. Special considerations are taken into account for fast generation of the CBFs, including the option of limiting near and far field interactions between CBFs and neighboring blocks, as well as introducing a sparse approximate inverse (SPAI) preconditioner specifically tailored to the CBFM [31]. The authors in [32] described a numerical technique focused on the analysis of radomes considering the MoM for the analysis of the antenna, and introducing macro-basis functions to describe the current distribution on the radome. In the present work, we generalize this technique including domain decomposition with two non-overlapping domains, one defined by the antenna analyzed using MLFMM with subdomains and the other the radome (including FSS) analyzed using MLFMM with CBFs. In addition, in the present work, we introduce a preconditioner for each domain problem. In the example included, we analyze the effect of the coupling between all the CBFs of the radome domain and considering only the coupling between neighboring CBFs.

This paper is organized as follows. Section 2 addresses the fundamentals of the developed approach. A test case including a complex radome is described and simulated in Section 3. Some conclusions and thoughts derived from the work presented in this document are finally presented in Section 4.

2. Description of the Numerical Technique

2.1. Separation of Antenna and Radome Domains

This section describes the electromagnetic and numerical treatment of the problem, considering a combination of MoM, MLFMA, and CBFM. In this paper, the low-level basis and testing functions considered are modified rooftops and razor blades defined on the parametric space of curved quadrilateral elements over NURBS (non-uniform rational B-spline) patches. The use of curved basis functions favors a better fit to the original surface, avoiding facetization errors. Figure 1 shows a scheme containing the described basis and testing functions. However, the approach described here can be applied to any other kind of basis and testing functions.

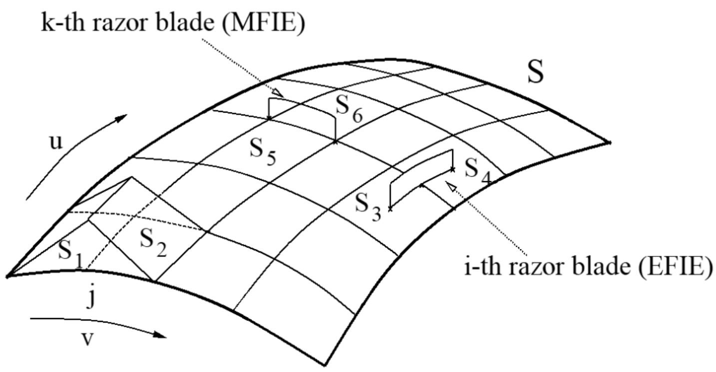

Figure 1. Basis and testing functions defined as curved rooftops and razor blades on a NURBS (non-uniform rational B-spline) patch.

As a first step, consider a separation of the scenario into two different domains: D_r refers to the radome domain and D_a indicates the antenna domain. Owing to the nature of radome structures, we will consider them non-overlapping in the present work. Figure 2 presents a generic 2D scheme of this decomposition.

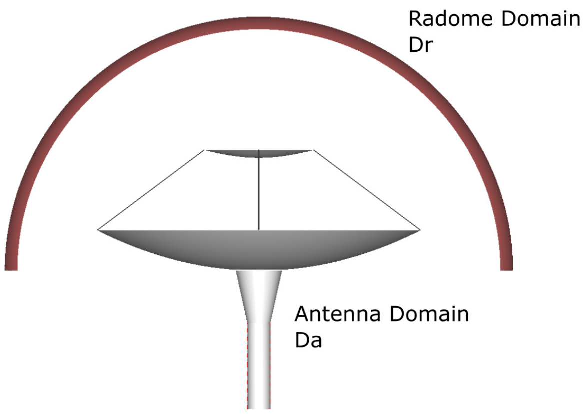

Figure 2. Separation of the antenna and radome domains.

The method of moments produces a linear system of equations that result from the transformation of a set of integro-differential equations defining the physics of the full problem:

$$[Z][J] = [V] \tag{1}$$

where $[Z]$ is the impedance matrix, $[J]$ is the current vector, and $[V]$ contains the excitation. Introducing the separation into both domains at this point, it is possible to expand Equation (1) as follows:

$$[Z] = \begin{bmatrix} [Z_{D_a,D_a}] & [Z_{D_a,D_r}] \\ [Z_{D_r,D_a}] & [Z_{D_r,D_r}] \end{bmatrix} \tag{2}$$

$$[J] = \begin{bmatrix} [J_a] \\ [J_r] \end{bmatrix} \tag{3}$$

$$[V] = \begin{bmatrix} [V_a] \\ [V_r] \end{bmatrix} \tag{4}$$

where $[Z_{D_1,D_2}]$ refers to the impedance sub-matrix where the active basis functions are contained in domain D_2 and the testing functions in D_1, with D_1 and D_2 being either D_a or $D_{r.}$ Note that Equations (2)–(4) are derived from Equation (1) and a subdivision of the matrix coefficients into different sub-matrices corresponding to both domains. The current and excitation vectors $[J]$ and $[V]$ are also expressed as the combination of two column vectors to the antenna and radome domains, as expressed by Equations (3) and (4).

2.2. Application of MLFMA and CBFM

For the sake of simplicity in this work, we will make use of the notation described above, although it is worthwhile to mention that, in turn, each impedance sub-matrix can be decomposed as a sum of its near-field and far-field terms:

$$[Z_{D_1,D_2}] = [Z^{(NF)}_{D_1,D_2}] + [Z^{(FF)}_{D_1,D_2}] \tag{5}$$

where, as previously indicated, D_1 and D_2 may refer to either domain. Equation (5) highlights the fact that, when applying the MLFMA, only the near field matrix is actually computed and stored, while the far field term is introduced into the iterative solution process by means of the aggregation, translation, and disaggregation of the multipole expansions [26]. In the rest of this paper, the implicit matrix-vector products will be understood as the separation of these two terms and application of the MLFMA.

The matrices involved in the previous expressions can be transformed owing to the use of the CBFM, which brings a new set of macro-basis functions that allows the reduction of the number of unknowns. First, an automatic division of the computational space in terms of cubic (or parallelepiped) volumes is performed. The typical size of a block spans one or a few wavelengths. The CBFs inside a block can be expressed as aggregations of the low-level basis functions contained in that block:

$$M^{(b)}_{i,k} = \sum_{j=1}^{N_k} \alpha^{(k)}_{i,j} T^{(k)}_i \tag{6}$$

$$M^{(t)}_{i,k} = \sum_{j=1}^{N_k} \alpha^{(k)}_{i,j} R^{(k)}_i \tag{7}$$

where $M^{(b)}_{i,k}$ and $M^{(t)}_{i,k}$ are the i-th basis and testing CBFs, respectively, defined on block k. The term $\alpha^{(k)}_{i,j}$ is the weight of the j-th low-level basis/testing function for that CBF. Finally, $T^{(k)}_i$ and $R^{(k)}_i$ are the i-th low-level basis and testing functions, respectively, on block k.

It can be mentioned at this point that, as seen in Equations (6) and (7), each CBF can be seen as a vector of weights, with each one applied to a specific low-level basis or testing function inside the block. The α weights in Equations (6) and (7) that define the CBFs need to be computed in a pre-processing stage. This is carried out by isolating each block, obtaining the currents induced from a set of plane waves surrounding it, and performing singular value decomposition (SVD) to extract a new base from all those induced currents. A threshold is imposed in order to truncate the number of CBFs retaining the singular vectors that correspond to the largest singular values. Figure 3 illustrates the CBF generation process as described above. From this point, we will make use of the matrices described by Equations (1)–(5) annotated with the prime operator to indicate that they refer to CBFs instead of low-level functions.

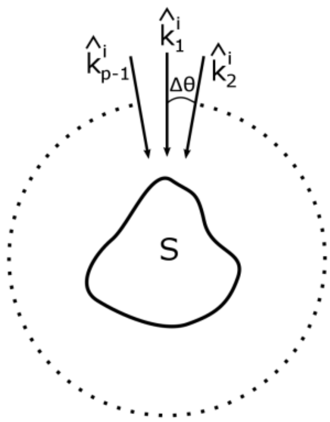

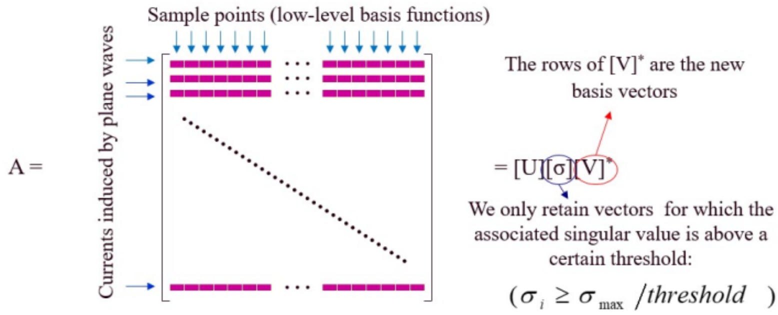

Figure 3. Scheme illustrating the procedure followed for the generation of the CBFs (charac-teristic basis functions).

2.3. Iterative Domain Decomposition Analysis

With the aforementioned considerations regarding domain separation as well as the application of MLFMA and CBFM, the iterative approach for the electromagnetic analysis can be described by the following steps, where n indicates the iteration number; $[V_a^{(n)}]'$ and $[V_r^{(n)}]'$ refer to the excitations on antenna and radome at the n-th iteration, respectively; and, analogously, $[J_a^{(n)}]'$ and $[J_r^{(n)}]'$ denote the currents on both domains for such an iteration:

1. Obtain the excitation over the antenna domain:

$$[V_a^{(1)}]' = [V_a]' \tag{8}$$

$$[V_a^{(n)}]' = [V_a]' - [Z_{D_a,D_r}]'^{[J_r^{(n-1)}]}, \text{ if } n > 1 \tag{9}$$

2. Obtain the current $\left[J_a^{(n)}\right]'$ on the antenna domain by solving iteratively (applying MLFMA):

$$[Z_{D_a,D_a}]'[J_a^{(n)}]' = [V_a^{(n)}]' \tag{10}$$

3. Obtain the field impressed on the radome domain $[V_r^{(n)}]'$ due to $[J_a^{(n)}]'$ as follows:

$$[Z_{D_r,D_a}]'[J_a^{(n)}]' = [V_r^{(n)}]' \tag{11}$$

4. Retrieve the current on the radome domain $[J_r^{(n)}]'$ by solving the following:

$$[Z_{D_r,D_r}]'[J_r^{(n)}]' = [V_r]' - [V_r^{(n)}]' \tag{12}$$

5. The total current distribution for the n-th iteration, as indicated by Equation (3) and expressed in terms of CBFs, is thus the following:

$$[J^{(n)}]' = \begin{bmatrix} [J_a^{(n)}]' \\ [J_r^{(n)}] \end{bmatrix} \tag{13}$$

Note that the use of a number of dielectric layers composing the radome, as well as the embedded FSS elements, can introduce bad convergence properties, which makes it desirable to consider techniques to counterbalance such a bottleneck. In the results presented in this work, a SPAI preconditioner specifically tailored to the CBFM [31] is applied. Equations (10) and (12) require solving iteratively two separate systems of equations, and the use of two separate SPAI preconditioning matrices previously computed. Additionally, an approximate variation of the method presented above can be derived by considering that the CBFs contained within each block only interact with those close to them, either in the same block (self-coupling approach) or in neighboring blocks in addition to the same block (neighboring coupling approach). The accuracy of these possible variations will be studied in the next section, which shows an example of the application of this technique, including the results for different interactions between both domains. We have found that three iterations yield very good accuracy for all the test cases carried out in the development of this work.

3. Numerical Results

This section provides a test case considering a complex scenario in order to validate the accuracy and computational efficiency of the method described in the previous sections. The simulations with which the approach presented in this work has been compared using the conventional MoM-MLFMA and named as such in several plots contained in this section were carried out using the commercial software Altair newFASANT, which has been extensively validated in the past. The scenario, shown in Figure 4, contains a Cassegrain reflector antenna fed by a conical horn, and this radiating system is covered by a hemispherical dome composed by two radomes: one at the top containing two dielectric layers with an FSS embedded within the inner interface (closest to the antenna), and a second radome at the bottom containing a single layer of dielectric. Both radomes are aligned, creating a perfectly smooth outer surface.

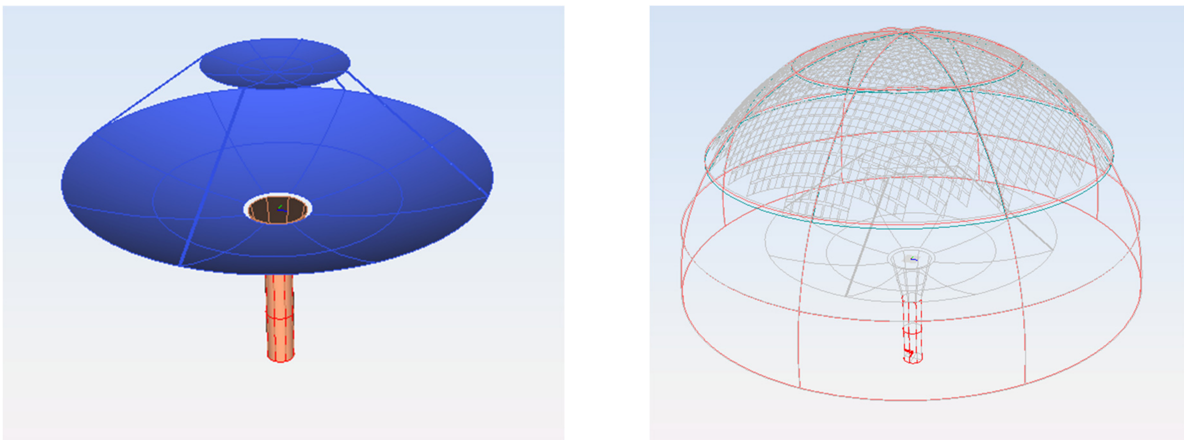

(**a**) (**b**)

Figure 4. Geometrical model of (**a**) antenna, containing a conical horn and a Cassegrain Reflector; (**b**) the full scenario, containing the antenna covered by a hemispherical dome built using a two-layered radome with a cross-shaped FSS embedded within the inner interface at the top, and a single layer radome at the bottom.

The diameter of the parabolic reflector is 200 mm and that of the hyperbolic sub-reflector is 67.2 mm. The working frequency is 14 GHz. The aperture of the conical horn is centered at the origin of coordinates and lays on the z = 0 plane. The vertex of the sub-reflector is located at z = 70 mm. There are four strips modeling supporting struts. The external diameter of the dome structure is 242 mm. The first radome extends from the tip of the dome at z = 121 mm down to z = 69.18 mm, and is composed of an inner layer of dielectric with a thickness of 1 mm, ε_r = 1.12, and tan δ = 0.002, and an outer layer with a thickness of 0.6 mm and ε_r= 4.3. The second radome extends from z = 69.18 mm down to z = 0 and contains a single layer of dielectric material matching the outer layer of the first radome, which makes the external surface of the dome structure continuous. There is an FSS on the inner interface of the first radome. This FSS was designed using the unit cell shown in Figure 5 on a planar layout and then projected onto the curved interface of the radome. The same figure shows the reflection and transmission coefficients of this FSS using the infinite periodic Green's function for a plane wave impinging in the $-\hat{z}$ direction and a frequency sweep ranging from 4 GHz to 24 GHz.

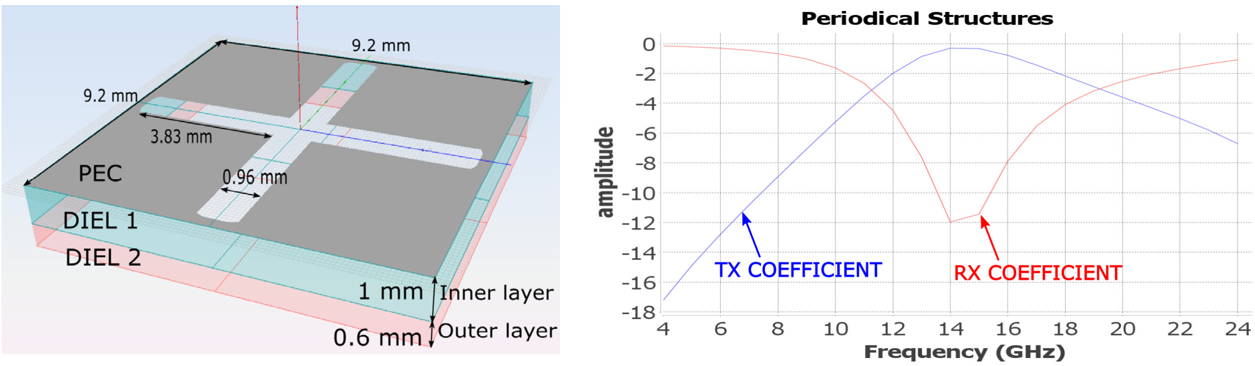

(**a**) (**b**)

Figure 5. (**a**) Geometrical scheme of the FSS (frequency selective surfaces) unit cell (planar); (**b**) re-flection and transmission coefficients on an infinite planar layout for a frequency sweep between 4 GHz and 24 GHz.

After mapping the FSS elements on a curved surface, the electromagnetic behavior of the structure can differ from that computed over an infinite planar layout. However, such a layout is a good starting point, allowing very fast simulations to design the unit cell. After projecting the FSS onto the curved interface, the resonance frequency may shift, which could require adjustments on the planar design (like cell scaling and so on). In many cases, such as that presented in this work, the curved design retains the frequential behavior originally desired and no further modifications are required.

The aforementioned test case was simulated using the conventional MoM-MLFMA approach as well as the technique proposed in this document, considering one, two, and three interactions between the antenna and radome domains following the iterative approach described in the previous section. The total number of NURBS surfaces used to model the scenario was 623. The number of low-level basis functions (rooftops) was 883,013. The number of blocks was 652 and the total number of CBFs was 153,899. The simulations were performed using a workstation containing two Intel Xeon E5-2690 processors with 128 GB of RAM and considering the electric field integral equation (EFIE) formulation. The sparse approximate inverse (SPAI) preconditioner [31] was applied in all the simulations performed, as well as the restarted generalized minimal residual method (GMRES) [33] to iteratively solve the systems of equations. Figure 6 shows the results for 181 observation directions along the $\varphi = 0°$ angular cut, ranging from $\theta = 0°$ to $\theta = 180°$. Some difference can be appreciated, especially at the lower field levels, as the number of iterations change. In the same figure, it is possible to see a comparison of the proposed approach with three iterations between domains and the conventional MoM-MLFMA, showing a very good agreement in the resulting radiation pattern.

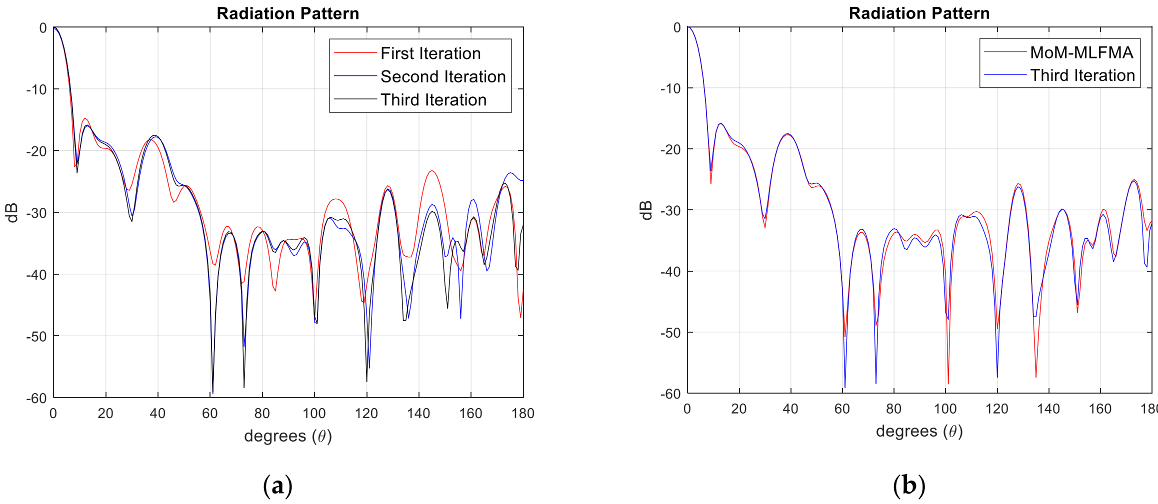

Figure 6. Radiation pattern results for the $\varphi = 0°$ angular cut: (**a**) comparison of the proposed ap-proach considering one, two, and three iterations between domains; (**b**) comparison between the proposed approach with three iterations between domains and MoM-MLFMA (method of moments with the multilevel fast multipole algorithm).

Figure 7 shows the results considering three iterations between domains, and the variations given using only the self-coupling blocks (left) and neighboring blocks (right). It is possible to see that, in this case, the accuracy is not good when only the coupling terms inside each block are used, while the results improve noticeably when introducing the coupling between adjacent blocks, although some differences at lower levels can be seen compared with the base, full-coupled algorithm with three iterations. The coupling distance has a noticeable effect in these simulations. While only considering the coupling between CBFs located in the same block presents noticeable disagreements, as seen in Figure 7a, the inclusion of adjacent blocks improves the accuracy to a degree that can be considered acceptable in many cases, with disagreements appearing about 30 dB under the maximum level.

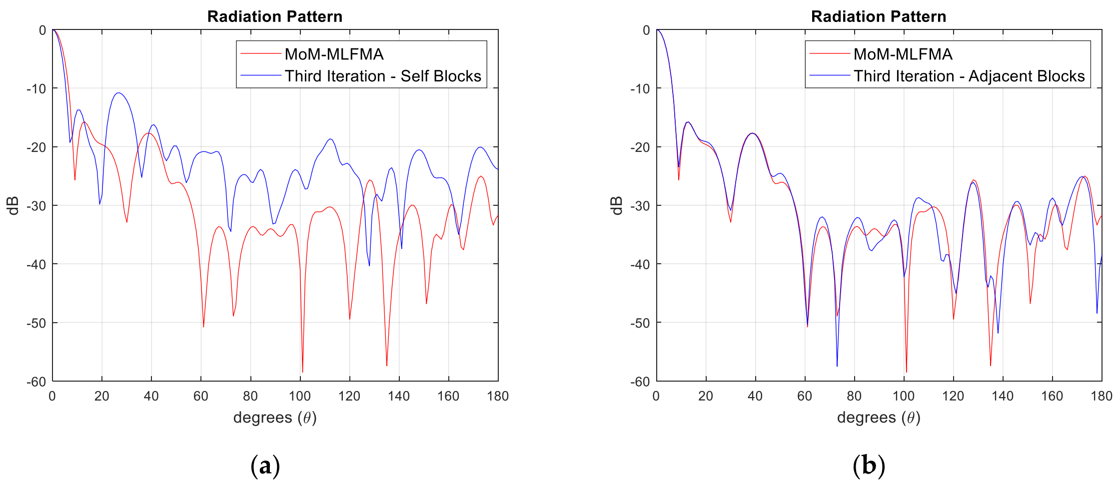

Figure 7. Radiation pattern results for the $\varphi = 0°$ angular cut: (**a**) considering the proposed approach with only self-block coupling and three iterations; (**b**) considering the proposed approach with self and neighboring block coupling and three iterations.

Some results comparing the analysis of the radome covering the antenna and the scenario containing only the antenna are provided in Figure 8. The presented radome introduces small insertion losses and boresight error and mainly affects the secondary lobes. Figure 8b shows, in turn, a frequency sweep of the gain results close to the resonance at 14 GHz, where it is possible to see that the FSS introduces the desired effect of serving as a passband filter centered at the working frequency. It shall be noted that the differences shown in Figure 8 are due to the effect of the placement of the radome, which mainly affects the width of the secondary lobe, introducing small insertion losses and a bandpass filtering effect as designed with the embedded FSS.

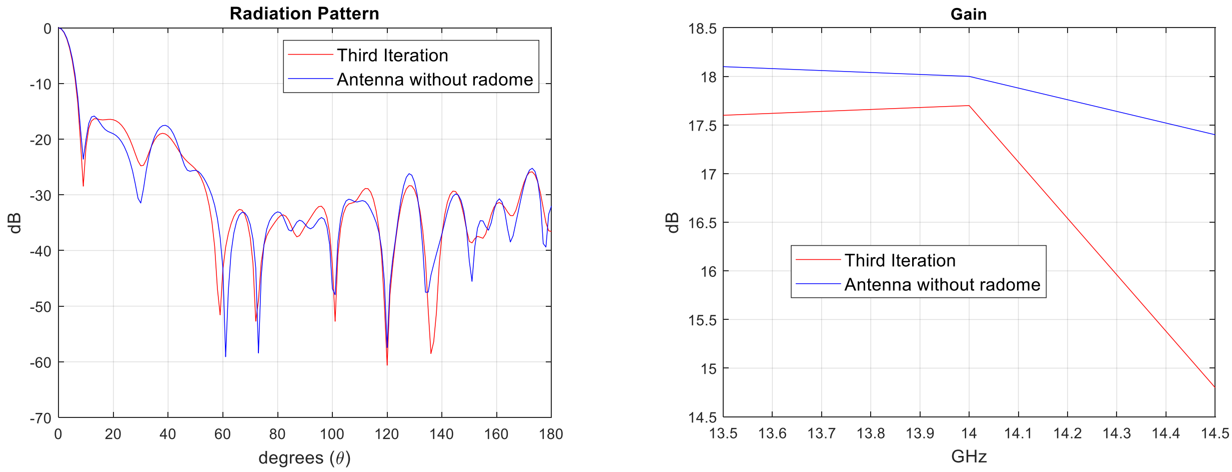

(**a**) (**b**)

Figure 8. (**a**) Radiation pattern results considering the radome with the antenna and compared with the antenna alone; (**b**) frequency sweep around the resonant frequency considering the radome with the antenna and the antenna alone, showing the frequency filtering characteristics of the embedded FSS.

Table 1 contains the CPU-time required to compute the analyses of this test case with MoM-MLFMA and the proposed approach with one, two, and three iterations between domains, and considering the workstation described at the beginning of this section. The times are broken down into the pre-processing stage (which in this case is considered to be the time required before the iterative solution process), the iteration stage, and the total simulation time. It can be seen that the extra pre-processing time required to compute the CBFs is compensated during the solution process when comparing MoM-MLFMM and the proposed approach. Additionally, the iteration time increases quite linearly as the number of iterations between both domains increases.

Table 1. Comparison of the CPU-time required by the proposed approach with one, two, and three iterations between domains, and MoM-MLFMA.

Approach	Pre-Processing Time [1] (s)	Iteration Time (s)	Total CPU-Time (s)
MoM-MLFMA (newFASANT)	13,586	27,964	41,550
Proposed approach, 1 iteration	17,670	4655	22,325
Proposed approach, 2 iterations	17,672	6650	24,320
Proposed approach, 3 iterations	17,672	9392	27,062

[1] Defined as the CPU-time elapsed before the iterative solution process.

4. Conclusions

The work presented in this document describes the development of a numerical analysis technique focused on complex radomes covering arbitrary antennas, by means of the separation of both domains (antenna and radome) and an iterative approach using macro-basis functions in order to ease the computational burden imposed by this kind of problem. We have found that this method performs efficiently compared with conventional alternatives with as few as three iterations between domains, offering good accuracy and convergence properties.

The results presented in this work validate the analysis technique proposed for the simulation of complex radomes using CBFM-MLFMA and a domain decomposition approach. The agreement is good compared with the conventional MoM-MLFMA results, obtaining a noticeable efficiency improvement in the solution process. In this and many other cases analyzed by the authors, three iterations between domains offer a very good compromise between accuracy and computational efficiency. Future research may include the study of techniques that may offer a further efficiency improvement, such as adaptively limiting the distance within which the CBFs are coupled. In this regard, it seems that self-coupling CBFs do not provide accurate results and neighboring coupling CBFs offer better results, although still not comparable to the base algorithm proposed.

An additional result from the work presented in this document was a fully parallelized computer tool for the analysis of radomes covering arbitrary antennas, which makes use of both shared and distributed memory paradigms (hybrid MPI/OpenMP approach) and can be executed on conventional computers, workstations, or large computing clusters.

Author Contributions: Conceptualization, C.D. and F.C.; Data curation, F.C.; Formal analysis, C.D.; Funding acquisition, C.D. and F.C.; Investigation, C.D.; Methodology, E.G.; Project administration, F.C.; Resources, F.C.; Software, C.D. and E.G.; Supervision, E.G.; Validation, E.G., and F.C.; Visualization, C.D.; Writing—original draft, C.D.; Writing—review & editing, C.D. All authors have read and agreed to the published version of the manuscript.

Funding: This work was supported in part by the Junta de Comunidad de Castilla-La Mancha (Project Ref. SBPLY/17/180501/000433); by the Universidad de Alcalá, project number CCG20/IA-063; and contracts ART.83 from Altair Inc. numbers REF.180/2019, 181/2019, and 183/2019.

Conflicts of Interest: The authors declare no conflict of interest.

References

1. Nair, R.U.; Jha, R.M. Analysis of Airborne Radomes: Trends and Perspectives. *IEEE Antennas Propag. Mag.* **2014**, *56*, 276–298. [CrossRef]
2. MacDonald, M.E. An Overview of Radomes for Large Ground-Based Antennas. *IEEE Aerosp. Electron. Syst. Mag.* **2019**, *34*, 36–43. [CrossRef]
3. Cady, W.M. *Radar Scanners and Radomes*; Ulan Press: Oxford, UK, 2012.
4. Althuwayb, A.A. Enhanced radiation gain and efficiency of a metamaterial inspired wideband microstrip antenna using substrate integrated waveguide technology for sub-6 GHz wireless communication systems. *Microw Opt Technol. Lett.* **2021**, *63*, 1892–1898. [CrossRef]
5. Elfergani, I.T.E.; Hussaini, A.S.; Rodriguez, J.; Abd-Alhameed, R. *Antenna Fundamentals for Legacy Mobile Applications and Beyond*; Springer: Cham, Switzerland, 2017; pp. 1–659.
6. Alibakhshi-Kenari, M.; Naser-Moghadasi, M.; Sadeghzadeh, R.A.; Virdee, B.S.; Limiti, E. A new planar broadband antenna based on meandered line loops for portable wireless communication devices. *Radio Sci.* **2016**, *51*, 1109–1117. [CrossRef]
7. Alibakhshi-Kenari, M.; Naser-Moghadasi, M.; Sadeghzadeh, R. The resonating MTM-based miniaturized antennas for wide-band RF-microwave systems. *Microw. Opt. Technol. Lett.* **2015**, *57*, 2339–2344. [CrossRef]
8. Shirkolaei, M.M. High Efficiency X-Band Series-Fed Microstrip Array Antenna. *Prog. Electromagn. Res. C* **2020**, *105*, 35–45. [CrossRef]
9. Alibakhshi-Kenari, M.; Virdee, B.S.; Azpilicueta, L.; Naser-Moghadasi, M.; Akinsolu, M.O.; See, C.H.; Liu, B.; Abd-Alhameed, R.A.; Falcone, F.; Huynen, I.; et al. A Comprehensive Survey of "Metamaterial Transmission-Line Based Antennas: Design, Challenges, and Applications". *IEEE Access* **2020**, *8*, 144778–144808. [CrossRef]
10. Mei, P.; Lin, X.Q.; Yu, J.W.; Zhang, P.C.; Boukarkar, A. A Low Radar Cross Section and Low Profile Antenna Co-Designed With Absorbent Frequency Selective Radome. *IEEE Trans. Antennas Propag.* **2018**, *66*, 409–413. [CrossRef]
11. Nair, R.U.; Jha, R.M. Electromagnetic Performance Analysis of a Novel Monolithic Radome for Airborne Applications. *IEEE Trans. Antennas Propag.* **2009**, *57*, 3664–3668. [CrossRef]
12. Kedar, A.; Revankar, U.K. Parametric Study of Flat Sandwich Multilayer Radome. *Prog. Electromagn. Res.* **2006**, *66*, 253–265. [CrossRef]
13. Zhou, L.; Pei, Y.; Fang, D. Dual-band A-sandwich radome design for airborne applications. *IEEE Antennas Wirel. Propag. Lett.* **2016**, *15*, 218–221. [CrossRef]
14. Costa, F.; Monorchio, A. A frequency selective radome with wideband absorbing properties. *IEEE Trans. Antennas Propag.* **2012**, *60*, 2740–2747. [CrossRef]
15. Omar, A.A.; Shen, Z. Thin 3-D Bandpass Frequency-Selective Structure Based on Folded Substrate for Conformal Radome Applications. *IEEE Trans. Antennas Propag.* **2019**, *67*, 282–290. [CrossRef]
16. Narayan, S.; Gulati, G.; Sangeetha, B.; Nair, R.U. Novel Metamaterial-Element-Based FSS for Airborne Radome Applications. *IEEE Trans. Antennas Propag.* **2018**, *66*, 4695–4707. [CrossRef]

17. Tricoles, G.P. Radome Electromagnetic Design. In *Antenna Handbook*; Springer: Boston, MA, USA, 1988; Volume 3, pp. 154–196.
18. Kozakoff, D.J. *Analysis of Radome-Enclosed Antennas*, 2nd ed.; Artech House: Norwood, MA, USA, 2010.
19. Wait, J.R. *Electromagnetic Waves in Stratified Media*, 1st ed.; Pergamon Press: Oxford, UK, 1970.
20. Knott, E.F. A Progression of High-Frequency RCS Prediction Techniques. *Proc. IEEE.* **1985**, *73*, 252–264. [CrossRef]
21. Men, H.; Dou, W. Hybrid IPO-BI-FEM for the analysis of 2D large radome with complex structure. *Microw. Opt. Technol. Lett.* **2009**, *51*, 1348–1353.
22. Li, L.W.; Leong, M.S.; Ma, X.; Yeo, T.S. Analysis of a circular aperture antenna and its covered dielectric hemispherical radome shell over ground plane: Near- and far-zone patterns. *Microw. Opt. Technol. Lett.* **1999**, *21*, 238–243. [CrossRef]
23. d'Elia, U.; Pelosi, G.; Pichot, C.; Selleri, S.; Zoppi, M. A physical optics approach to the analysis of large frequency selective radomes. *Prog. Electromagn. Res.* **2013**, *138*, 537–553. [CrossRef]
24. Kim, J.H.; Chun, H.J.; Hong, I.P.; Kim, Y.J.; Park, Y.B. Analysis of FSS Radomes Based on Physical Optics Method and Ray Tracing Technique. *IEEE Antennas Wirel. Propag. Lett.* **2014**, *13*, 868–871.
25. Harrington, R.F. *Field Computation by Moment Methods*; McMillan: New York, NY, USA, 1968.
26. Song, J.M.; Chew, W.C. Multilevel Fast Multipole Algorithm for Solving Combined Field Integral Equations of Electromagnetic Scattering. *Microw. Opt. Technol. Lett.* **1995**, *10*, 14–19. [CrossRef]
27. Garcia, E.; Delgado, C.; Lozano, L.; Gonzalez, I.; Catedra, F. An efficient hybrid-scheme combining the characteristic basis function method and the multilevel fast multipole algorithm for solving bistatic RCS and radiation problems. *Prog. Electromagn. Res. B* **2011**, *34*, 327–343. [CrossRef]
28. Delgado, C.; Catedra, F. Efficient Generation of Macro Basis Functions for Radiation Problems Using Ray-Tracing Derived Dynamic Thresholds. *IEEE Antennas Wirel. Propag. Lett.* **2018**, *17*, 849–852. [CrossRef]
29. Delgado, C.; Catedra, F. Combination of ray-tracing and the method of moments for electromagnetic radiation analysis using reduced meshes. *J. Comput. Phys.* **2018**, *361*, 412–423. [CrossRef]
30. Delgado, C.; Garcia, E.; Catedra, F. Hybrid Iterative Approach Combined with Domain Decomposition for the Analysis of Large Electromagnetic Problems. *Proc. IEEE* **2013**, *66*, 320–331. [CrossRef]
31. Delgado, C.; Catedra, F. Sparse Approximate Inverse Preconditioner with Parametric Sparsity Pattern Applied to the Macrobasis Function Methods. *IEEE Antennas Wirel. Propag. Lett.* **2018**, *17*, 849–852. [CrossRef]
32. García, E.; Delgado, C.; Cátedra, F. Efficient Iterative Analysis Technique of Complex Radome Antennas based on the Characteristic Basis Function Method. *IEEE Trans. Antennas Propag.* **2021**, in press. [CrossRef]
33. Saad, Y.; Schultz, M.H. GMRES: A generalized minimal residual algorithm for solving nonsymmetric linear systems. *SIAM J. Sci. Stat. Comput.* **1986**, *7*, 856–869. [CrossRef]